Chemical Science

ROYAL SOCIETY OF CHEMISTRY

EDGE ARTICLE

View Article Online
View Journal | View Issue

Cite this: *Chem. Sci.*, 2024, **15**, 15737

All publication charges for this article have been paid for by the Royal Society of Chemistry

Received 24th May 2024
Accepted 25th August 2024

DOI: 10.1039/d4sc03415e

rsc.li/chemical-science

Directional growth and reconstruction of ultrafine uranium oxide nanorods within single-walled carbon nanotubes†

Luyao Zhang,[a] Kun Wang,[a] Xin Zhao,[a] Guoping Yang,[b] Yulong Jiang[a] and Feng Yang *[a]

Understanding the atomic structures and dynamic evolution of uranium oxides is crucial for the reliable operation of fission reactors. Among them, U_4O_9—as an important intermediate in the oxidation of UO_2 to UO_{2+x}—plays an important role in the nucleation and conversion of uranium oxides. Herein, we realize the confined assembly of uranyl within SWCNTs in liquid phase and reveal the directional growth and reconstruction of U_4O_9 nanorods in nanochannels, enabled by *in situ* scanning transmission electron microscopy (STEM) e-beam stimulation. The nucleation and crystallization of U_4O_9 nanorods in nanochannels obey the "non-classical nucleation" mechanism and exhibit remarkably higher growth rate compared to those grown outside. The rapid growth process is found to be accompanied by the formation and elimination of U atom vacancies and strain, aiming to achieve the minimum interfacial energy. Eventually, the segments of U_4O_9 nanorods in SWCNTs merge into single-crystal U_4O_9 nanorods *via* structural reconstruction at the interfaces, and 79% of them exhibit anisotropic growth along the specific ⟨110⟩ direction. These findings pave the way for tailoring the atomic structures and interfaces of uranium oxides during the synthesis process to help improve the mechanical properties and stability of fission reactors.

Introduction

Uranium dioxide (UO_2) with a fluorite structure is currently the most widely used and intensively studied nuclear fuel for the generation of electricity.[1,2] The oxidation of UO_2 is important for the processes involved in nuclear fuel fabrication and handling, as well as for understanding fuel changes during reactor operation and predicting the chemical chemistry of spent fuel.[3] During in-service reactor operation, UO_2 easily undergoes oxidation at high temperature and forms UO_{2+x} with complicated structures and phases, such as U_4O_9, U_3O_8, and UO_3,[4] thereby affecting the mechanical properties and stability of fuel rods. U_4O_9, considered to be an important intermediate, plays a key role in the phase transition from UO_2 to U_3O_8.[5] Therefore, preparing phase-pure intermediate U_4O_9 oxides and gaining insights into their complex nucleation and growth processes at the atomic level are essential for understanding the conversion process between various uranium oxides.

Crystal nucleation plays important roles in controlling the atomic structures, surface/interfaces, and properties of nanomaterials.[6,7] Classical crystal nucleation theory, derived from the thermodynamic process, identifies the direct aggregation of monomers into a new thermodynamic phase by a single-step process.[8] However, numerous experimental observations proved that the formation of a thermodynamically stable phase proceeds through multiple steps, involving the initial formation of cluster intermediates—known as nonclassical nucleation theory.[9–11] Despite achievements in nucleation theories, crystal nucleation such as biomineralization often occurs in a microenvironment, such as surfaces, channels, or pores, rather than in bulk solution,[12] which are necessary to guide the nucleation and growth. Single-walled carbon nanotubes (SWCNTs), as a 1–2 nm-size nanoreactor without any dangling bonds,[13,14] provide an ideally homogeneous environment to ensure the uniformity of reactions, which is highly suitable for investigating mass transport[15–17] and chemical reactions[18–20] in nanochannels. SWCNTs with unique internal cavities have also been widely used for the fabrication of various one-dimensional (1D) nanomaterials, such as single-atomic chains,[21–23] molecules,[17] clusters,[24–31] and nanowires.[32–40] Moreover, the conductive single-graphite shell of SWCNTs not only prevents degradation of the internal structure by transporting the e-beam electrons away but also benefits TEM observation at the

[a]*Department of Chemistry, Southern University of Science and Technology, Shenzhen, Guangdong 518055, China. E-mail: yangf3@sustech.edu.cn*

[b]*Jiangxi Key Laboratory for Mass Spectrometry and Instrumentation, Jiangxi Province Key Laboratory of Synthetic Chemistry, East China University of Technology, Nanchang 330013, China*

† Electronic supplementary information (ESI) available. See DOI: https://doi.org/10.1039/d4sc03415e

atomic scale,[41] making them suitable for investigating radioactive species such as uranium protected by tube walls.

The development of advanced *in situ* transmission electron microscopy (TEM) has enabled direct atomic-level observation of the dynamic structural evolution of nanomaterials,[6,7,42,43] which is beneficial for further revealing the underlying growth and catalysis mechanisms.[44–53] Onofri *et al.* found from *in situ* TEM that when irradiated UO_2 polycrystalline films were heated to 1400 °C, all irradiation-induced defects (dislocation lines and dislocation loops) were repaired at 1000–1100 °C, with the dislocations disappearing mainly by creep and the dislocation loops disappearing by sliding in the ⟨110⟩ direction.[1] These attempts pave the way for providing more opportunities to reveal the growth mechanisms and structural evolution of uranium-based nanomaterials.

Herein, we realize the confined assembly and preparation of ultrafine U_4O_9 nanorods within SWCNTs. Stimulated by a low-dose e-beam equipped in an aberration-corrected scanning TEM (STEM), the complete crystallization processes of U_4O_9 nanorods from amorphous UO_x in SWCNT channels are comprehensively revealed. The detailed growth behaviors of U_4O_9 nanorods within SWCNT channels, including anisotropic growth along a specific crystal direction, evolution of strain and U atom vacancies, and structural reconstruction, are revealed through atomic-scaled *in situ* STEM and statistical analyses. These *in situ* findings may help us understand the oxidation dynamics and mechanical evolution of uranium oxides.

Results and discussion

Confined assembly of uranyl and growth of U_4O_9 nanorods in SWCNTs

Uranyl ($^{238}UO_2(acac)_2$) was confined within SWCNTs (denoted as $UO_2(acac)_2$@SWCNTs) *via* a two-phase self-assembly method (see the Experimental section). The e-beam of STEM was utilized to decompose and reduce $UO_2(acac)_2$, resulting in the formation of U_4O_9 nanorods within SWCNTs (denoted as U_4O_9@SWCNTs). The electrons from the e-beam act as a reducing agent to stimulate the reduction of $UO_2(acac)_2$ and simultaneously trigger the crystallization of U_4O_9 nanorods. To quantify the crystallization rate of uranium oxides and minimize radiation damage, the e-beam intensity was precisely controlled to range from 0.06 to 0.07 nA, ensuring atomically spatial and millisecond temporal resolution (Fig. S1†). When the e-beam intensity was higher than 0.1 nA, the nucleation rate of the nanocrystals was too fast and the nanocrystals were easily damaged by the e-beam (Fig. S1†), affecting the processes of nucleation and growth as well as the evolution of defects.

Typical high-angle annular dark field STEM (HAADF-STEM) images and energy dispersive X-ray (EDX) elemental mapping provide direct evidence that uranyl was uniformly confined within the SWCNTs (Fig. 1a–c). The uranyl aggregated on the outer surface of SWCNTs was efficiently removed by washing with *N*,*N*-dimethylformamide (DMF) three times, while the confined uranyl within the SWCNTs was retained. The atom-resolved HAADF-STEM images and corresponding fast Fourier transform (FFT) patterns show well-crystalized nanorods with a width of 10–20 Å within the SWCNTs. Both HAADF-STEM and high-resolution TEM (HRTEM) images with the nanotube wall visible indicate the encapsulation of U_4O_9 nanorods in SWCNT channels (Fig. S2†). The face-centered-cubic (fcc) U_4O_9 (space group: $F\bar{4}3m$) orientations projected along typical [112], [110], [111], and [001] zone axes are consistent with the superimposed models (Fig. 1d–g and S3†). STEM combined with FFT was used to statistically analyse the growth direction of U_4O_9 nanorods in the SWCNTs. 79% of U_4O_9 nanorods grow along the $\langle 1\bar{1}0\rangle$ direction, and 14% of them grow along the $\langle 1\bar{1}1\rangle$ direction within the SWCNTs (Fig. 1h). The preferential growth could be ascribed to two factors. First, the value of directional anisotropy (Λ_a) has generally been used to evaluate the preferential growth of 1D crystals. It has been reported that the value of Λ_a $\langle 1\bar{1}0\rangle$ is much larger than that of ⟨001⟩, so the growth rate along the $\langle 1\bar{1}0\rangle$ direction is faster.[54,55] Hence, the adatom diffusion of U preferentially occurs along the $\langle 1\bar{1}0\rangle$ direction, thus allowing 1D nanorods to grow. Second, the crystal growth along the $\langle 1\bar{1}0\rangle$ direction minimizes structural stress, allowing the crystal to grow continuously along the longitudinal axis.[56] To further determine the thickness of confined U_4O_9 nanorods, annular dark field (ADF) intensity files were used to analyse the U atomic columns in an ordered lattice. The thickness of U_4O_9 nanorods was estimated to be approximately 5–6 U atoms, indicating the ultrathin structure (Fig. S4†).

To compare the structures and orientations of uranium oxide formed by heating and electron beam stimulation, we performed *ex situ* STEM characterization of $UO_2(acac)_2$@SWCNTs that had been annealed in a tube furnace at 600 °C under H_2/Ar. The *ex situ* HAADF-STEM images show that the confined nanowires also display a U_4O_9 structure, with 97% of them preferentially growing along the $\langle 1\bar{1}0\rangle$ direction (Fig. S5†). These results are similar to those acquired using *in situ* TEM e-beam stimuli.

Nucleation and crystallization of uranium oxides within SWCNTs

To track the nucleation process of U_4O_9 nanorods inside SWCNTs, time-sequential HAADF-STEM images were recorded to depict the growth trajectory. Fig. 2a and S6† show the typical nucleation processes of typical U_4O_9 nanorods in 150 s. Three distinguishable stages of U_4O_9 nanorod formation can be identified. In the initial stage (0–20 s), the amorphous $UO_2(acac)_2$ nanowires shrink rapidly under e-beam stimulation, due to the coalescence and aggregation of U and O atoms into denser UO_x. A metastable species featuring an amorphous structure may exist on the surface of the nanostructures before the full crystallization of nanorods. In the second stage (20–40 s), *in situ* observation revealed the gradual appearance of lattice fringes in amorphous UO_x as the reaction proceeded. The typical feature of this stage is the crystallization of metastable UO_x, with the formation of multiple interfaces (defects). Finally, the U_4O_9 nanorods were fully crystalized and merged at 40–150 s. The short nanorod segments in the same SWCNT channel gradually ripen into single-crystals and poly-crystals *via* atomic reconstruction at the interface at 150 s, analogous to the Ostwald ripening and orientation attachment reported elsewhere.[57]

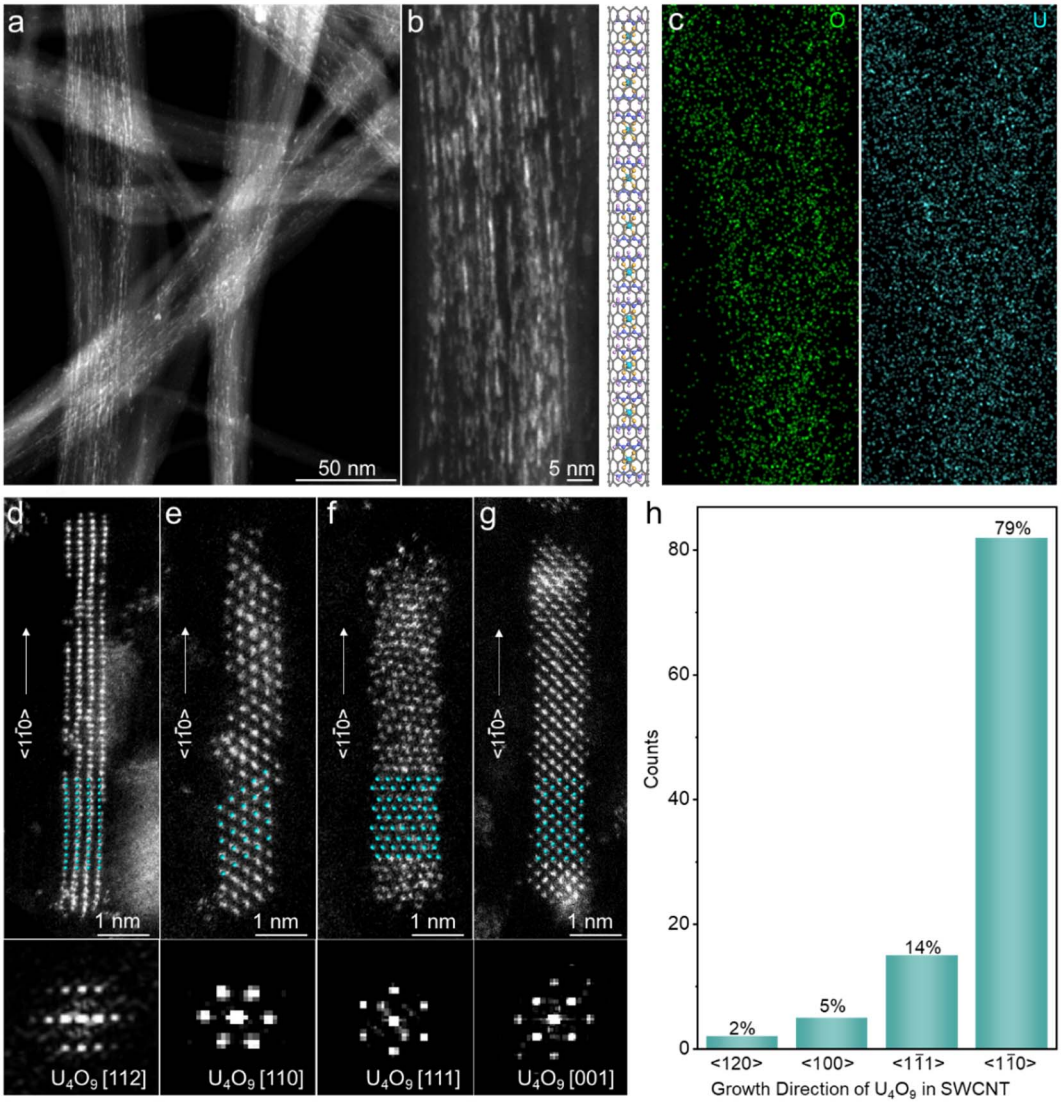

Fig. 1 Encapsulation of uranyl and directional growth of U_4O_9 within SWCNTs by e-beam stimulation. (a and b) HAADF-STEM images and model of $UO_2(acac)_2$@SWCNTs. (c) EDX mapping of U and O elements. (d–g) Aberration-corrected HAADF-STEM images and corresponding FFTs of U_4O_9 nanorods along different zone axes. The superimposed U_4O_9 atomic models (O atoms are invisible) and the growth directions of U_4O_9 nanorods are also shown. (h) Statistics of growth directions of U_4O_9 nanorods along the SWCNT axis based on STEM image analysis.

To capture the dynamic process with a higher time resolution, an e-beam stimuli experiment was also carried out on an *in situ* aberration-corrected TEM. The time-sequential HRTEM images show that the amorphous UO_x gradually crystallizes to form U_4O_9 nanorods in SWCNTs (Fig. S7†), which is similar to the result acquired using *in situ* STEM stimuli.

The length of the nanorods for different e-beam stimulation times is illustrated in Fig. 2b, which is derived from the above HAADF-STEM images. The length of all observed nanowires gradually shrinks by approximately 30% during the crystallization process and remains stable after full crystallization. Evaluating the full crystallization time of U_4O_9 nanorods within SWCNTs shows that the full-crystallization time decreases with decreasing length of U_4O_9 nanorods (Fig. 2b). This may arise from two critical factors. First, the growth and crystallization of short U_4O_9 nanorods require a shorter atomic diffusion path and less atom feeding than those of long nanorods. Second, the appearance of defects is inevitable during the crystal growth process. Shorter nanorods are more likely to minimize defects through self-healing mechanisms owing to their shorter atomic diffusion path, thereby reaching a single-crystal more easily than longer nanorods. Besides, it is found that the confined U_4O_9 nanorods generally experience a shorter crystallization time (<2 min) than those on the outer surface of SWCNTs (56 min), given the similar size of U_4O_9 (Fig. S8†). The accelerated growth rate could be induced by the SWCNTs nanoconfinement effect: the unique 1D 1 nm-size cavity of SWCNTs restricts the random motion of U and O atoms, leading to their preferential aggregation and nucleation along the 1D tube axis, thus accelerating the growth rate of U_4O_9 nanorods in SWCNTs.

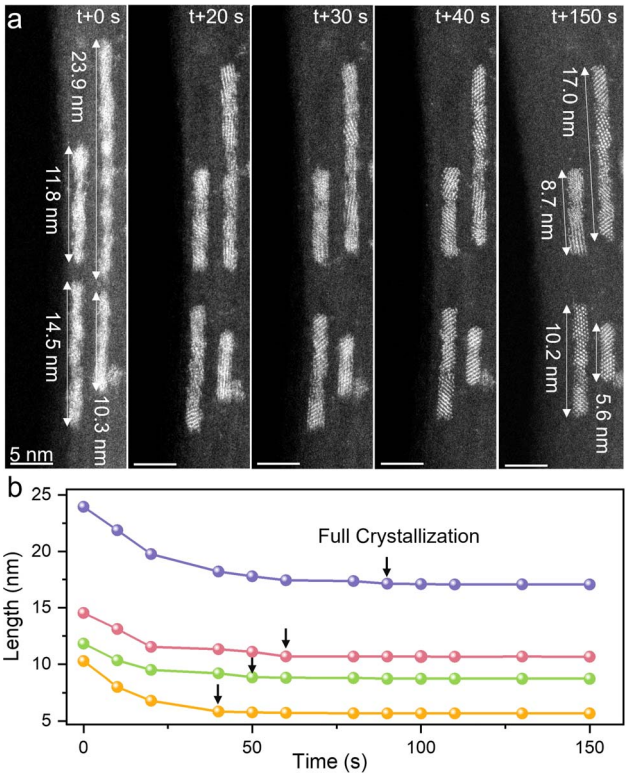

Fig. 2 *In situ* STEM observation of the growth process of U_4O_9 nanorods in SWCNTs stimulated by an e-beam. (a) Time-sequential HAADF-STEM images of U_4O_9 formed at different stages. (b) The length of U_4O_9 nanorods *versus* irradiation time derived from analysis of STEM images. The full crystallization time for each U_4O_9 nanorod is marked by arrows.

Strain and interface evolution during the growth of U_4O_9 nanorods within SWCNTs

In addition to crystallization-dependent length contraction, the atomic-scaled structural evolution of U_4O_9 nanorods associated with the strain and interface within SWCNTs was revealed by *in situ* STEM. Fig. 3 shows the atomic-scaled HAADF-STEM images and corresponding atomic models of the structural evolution from amorphous UO_x to crystallized U_4O_9 nanorods. At 0–20 s, two U_4O_9 segments with the same orientation of [110] partially crystallized from the two ends of amorphous UO_x, with a dislocation interface between them (Fig. 3a–c, marked by solid white lines). Then, the U_4O_9 [110] on the top of the nanorod was reconstructed to the [130] orientation at 30 s and further to the [110] orientation at 40 s; the dislocation interface was eliminated when two U_4O_9 segments coalesced into a long single-crystal nanorod (Fig. 3d and e). The surfaces of two adjoining segments at the interface made transient contact at multiple points, which further coalesced to reduce mutual surface energies before growing together.[58,59]

It is also obvious that the formation of a dislocation interface is accompanied by the appearance of surface strains and atomic vacancies in the U_4O_9 nanorods. When the dislocation interface evolved from 10 to 30 s, U_4O_9 with a bent lattice plane was notably observed in the HAADF-STEM images, indicating lattice strain (Fig. 3c and d, marked by curved dashed lines). The shear strain maps of ε_{xy} derived from geometric phase analysis (GPA)[60] further confirmed the distribution of lattice strain in the U_4O_9 nanorods. When the lattice plane was bent, most of the regions showed high strain with a red color; when the crystal was straightened, the regions changed to green color, indicating that the strain was released (Fig. S9†). The lattice strain eventually disappeared with the elimination of the dislocation interface at 40 s; that is, two U_4O_9 segments coalesced into a single-crystal nanorod with continuous lattice fringes (Fig. 3e, marked by straight dashed lines). More STEM results showing similar lattice strain during the growth of U_4O_9 are shown in Fig. S10,† indicating the generality of the observation. Lattice strain in ultrafine U_4O_9 nanorods could be induced by the lattice mismatch at the dislocation interface: that is, two U_4O_9 segments linked with different orientations.

The evolution of lattice strain is also accompanied by the formation and healing of U atom vacancies. The ADF intensity profiles across the same atomic column in the projection of U_4O_9 nanorods show lower intensities when the lattice strain emerged at 20–30 s, compared with that at 10 s, indicating the formation of U vacancies (Fig. 3g, marked by arrows). When two U_4O_9 nanorods merged into a single-crystal nanorod with the release of strain at 40 s, the same atomic vacancies were healed again by migrating U and O atoms (Fig. 3g, marked by arrows). These results imply that formation and healing of U atom vacancies are associated with strain generation and release to ensure the minimum interfacial energy.

We further conducted statistical analyses based on numerous HAADF-STEM images and ADF intensity profiles to investigate the crystal-plane-dependent atomic defects. After crystallization, 98% (116 of 118) of observed U_4O_9 nanorods exposed lattice planes of (110), (112), (130), (111), (100), and (332) (Fig. 4c, blue pillars). Among them, the U atom vacancies, appearing in the body of the nanorods, mainly existing on the crystal planes (111), (100), and (332) but were invisible on other exposed lattice planes (Fig. 4a–c, pink pillars). More HAADF-STEM images showing such lattice-plane-dependent exposure of U atom vacancies are shown in Fig. S11 and S12.† This selective exposure of U atom vacancies, depending on crystal planes, could be associated with surface energy, implying that the U and O atoms might find it more difficult to diffuse on (111), (100), and (332) planes than on other crystal planes, resulting in the formation of a vacant U column.

We further performed electron energy loss spectroscopy (EELS) with nanometer spatial resolution[61–63] to reveal the electronic structures of U_4O_9 with and without atomic U vacancies. The EELS spectra show that U_4O_9 with atomic U vacancies displays a 1.5 eV upshift in the U $O_{4,5}$-edge compared to U_4O_9 without atomic vacancies, while the C K-edge as a reference does not change (Fig. 4d). This result indicates that U_4O_9 with defects exhibits a higher U valence state than that without defects, which could be ascribed to U atomic vacancy induced electron delocalization[64] around the U atom, thereby resulting in a higher valence state for the U atoms.

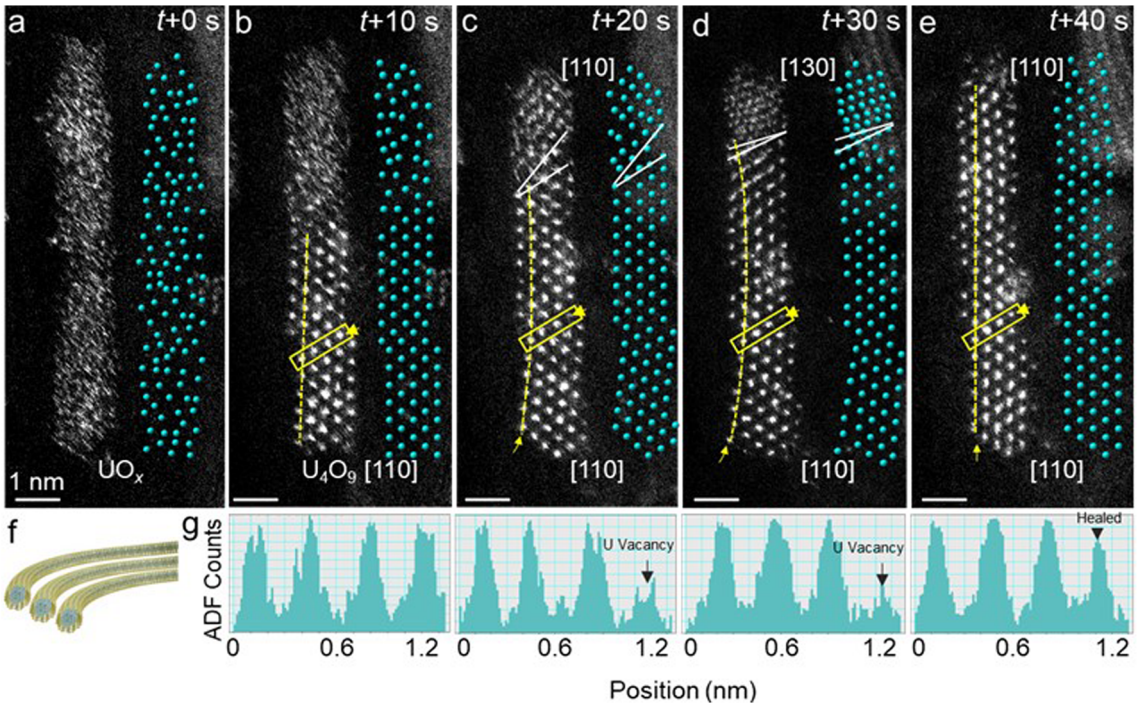

Fig. 3 Atomic-scale strain and interface evolution during the nucleation of U_4O_9 nanorods in SWCNTs. (a–e) Time-sequential HAADF-STEM images of the typical interface formation process and the corresponding interfacial atomic models. (f) Schematic illustration of the structure of amorphous UO_x@SWCNTs. (g) ADF intensity profiles of atomic columns showing the U atomic vacancies in U_4O_9 nanorods, which are marked by arrows. The dashed lines and curves in (b–e) only serve as guides to the eyes.

Reconstruction-assisted crystallization of single-crystal U_4O_9 nanorods

We further conducted *in situ* STEM to reveal the atomistic pathway of formation of single-crystal U_4O_9 nanorods *via* structural reconstruction of U_4O_9 segments (Fig. 5). The interface between two adjacent U_4O_9 segments (top and bottom regions) is marked by the dashed line. At the initial stage (0 s), two U_4O_9 segments orient along different zone axes of $[112]_{top}$ and $[332]_{bottom}$, connected by the lattice planes of $(\bar{1}10)_{top}$ and $(1\bar{3}3)_{bottom}$ without any lattice matching (Fig. 5a and e). At 30 s, the two U_4O_9 segments reconstruct to $[332]_{top}$ and $[112]_{bottom}$, respectively (Fig. 5b and f). At 30–60 s, the top [332] U_4O_9 segment continues to reconstruct to the [111] orientation, while the bottom one remains unchanged (Fig. 5c and g). Finally, the top [111] U_4O_9 segment further reconstructs to the [112] orientation and eventually aligns and merges with the bottom [112] U_4O_9 segment at 80 s, forming a single-crystal nanorod (Fig. 5d and h). Notably, the interface between the top and bottom segments moves slightly (Fig. 5a–c, marked by dashed lines).

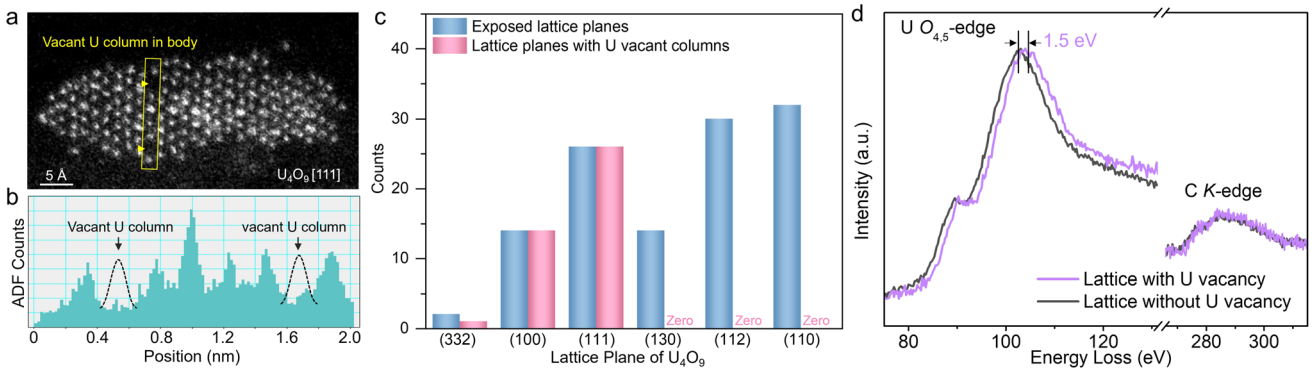

Fig. 4 Crystal-plane-dependent exposure of U atomic vacancies in U_4O_9 nanorods. (a and b) HAADF-STEM images and the corresponding ADF intensity profile showing the U vacant columns in the body (marked by arrows). (c) Statistics of exposed lattice planes and lattice planes with U vacant columns after e-beam irradiation of U_4O_9 nanorods for 10 min. The total numbers of random exposed lattice planes and lattice planes with vacant U columns are 118 and 41, respectively. (d) Normalized EELS spectra of U $O_{4,5}$-edge and C K-edge acquired from a U_4O_9 lattice with and without atomic U vacancies.

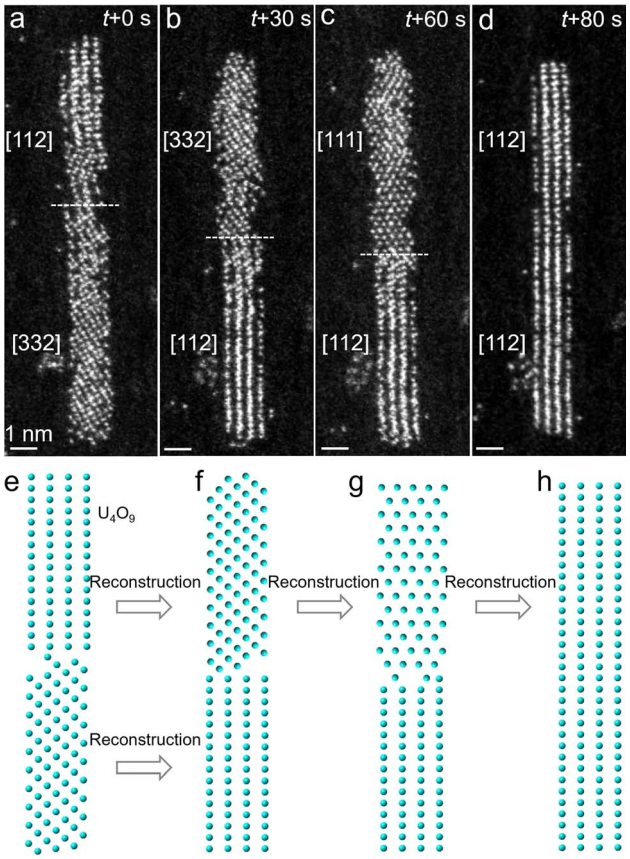

Fig. 5 Structural reconstruction-assisted growth of single-crystal U_4O_9 nanorod within an SWCNT. (a–d) Time-sequential HAADF-STEM images. (e–h) Corresponding atomic models of U_4O_9 reconstruction processes derived from STEM images. The O atoms are invisible.

This indicates that the atoms reconstruct at the interface due to the interaction between two segments, aiming to reduce the interfacial energy and achieving structural relaxation. As the e-beam stimulus time is further prolonged to 10 min, no obvious rotation or lattice distortion is observed (Fig. S13†), demonstrating the high stability of single-crystal U_4O_9 nanorods.

This reconstruction-assisted crystallization of single-crystal U_4O_9 nanorods could be induced by the unique confining effect of SWCNTs, due to the strictly restricted motion of a segment within the 1 nm-SWCNT-channel. More *in situ* STEM results depicting the similar reconstruction-induced formation of single-crystal U_4O_9 nanorods are shown in Fig. S14,† demonstrating the generality of the observation.

Conclusion

We realized the confined assembly and preparation of ultrafine U_4O_9 nanorods within SWCNTs. Stimulated by a low-dose STEM e-beam, we directly revealed the complete crystallization processes of U_4O_9 nanorods from amorphous UO_x in SWCNT channels. The crystallization of U_4O_9 nanorods obeys the "non-classical nucleation" mechanism, which shows a faster crystallization rate in SWCNTs than those on the outer surface of SWCNTs, due to the restricted motion of U and O atoms in a 1D channel. 79% of U_4O_9 nanorods exhibit anisotropic growth along the specific $\langle 1\bar{1}0 \rangle$ direction owing to their large directional anisotropy (A_a). The nucleation and crystallization of U_4O_9 nanorods are accompanied by the formation and healing of the U atom vacancies, which are associated with strain generation and release to ensure the minimum interfacial energy. The U_4O_9 lattice with atomic vacancies exhibits a higher U valence state than that without vacancies. Eventually, the segments of U_4O_9 nanorods in SWCNTs merge to form single-crystal U_4O_9 nanorods *via* structural reconstruction at interfaces. This direct visualization of growth trajectories of U_4O_9 nanorods in a 1 nm channel provides a comprehensive understanding of the growth mechanisms and structural evolution of uranium oxides at the atomic scale, which may help improve the mechanical properties of fuel rods and promote their resistance to O_2 oxidation.

Experimental

Confined assembly of $UO_2(acac)_2$ within SWCNTs

Tuball-SWCNTs (tube diameter = 0.9–2.2 nm) were purchased from OCSiAl company. Typically, 40 mg of SWCNTs were dispersed in 20 mL of deionized water and stirred for 4 h at room temperature. Subsequently, 200 μL of a DMF solution containing 10 mg of uranyl ($^{238}UO_2(acac)_2$) was added to the above mixture and stirred for 48 h. Subsequently, the $UO_2(acac)_2$@SWCNTs were centrifuged and dried in a vacuum oven for 12 h. The dried samples were washed with DMF and deionized water three times each and then dried in a vacuum oven for 12 h.

Preparation of TEM specimens

The $UO_2(acac)_2$@SWCNTs was dispersed in 5 mL of ethanol and sonicated for 10 min. 2 μL of the suspension was then dropped onto lacey-carbon Cu TEM grids and dried in air before *in situ* S/TEM experiments.

Aberration-corrected TEM and STEM e-beam stimuli experiments

The STEM e-beam stimuli experiment was carried out using an FEI Titan Cubed Themis 60–300 (operated at 300 kV) equipped with a high-brightness electron gun, a spherical aberration (C_S) probe and an image corrector, capable of recording high-resolution STEM images with a spatial resolution of ~60 pm. Dark field STEM images were acquired with an ADF detector with a probe convergence angle of 25 mrad and a collection angle of ~48–200 mrad. During the experiments, the samples were irradiated with an e-beam intensity of 0.06 or 0.07 nA for durations ranging from 5 to 30 min.

The TEM e-beam stimuli experiment was conducted on an aberration-corrected Titan G2 80–300 ETEM with an objective lens spherical aberration corrector. The transformation of $UO_2(acac)_2$@SWCNTs to U_4O_9 nanorods within SWCNTs was captured using a Gatan OneView camera in *in situ* mode at a speed of 25 fps with a frame size of 4k × 4k pixels. The e-beam intensity is consistent with that used for STEM e-beam stimuli.

STEM-EELS characterization

EELS was acquired on an aberration-corrected STEM (FEI Titan Cubed Themis G2) equipped a GIF Quantum ERS (1304) EELS spectrometer with an energy dispersion of 1.0 eV and operated at an acceleration voltage of 300 kV. The zero-loss EELS spectrum was acquired simultaneously in dual-EELS mode. The spectra were acquired after background subtraction from the raw EELS spectra using the linear combination of power laws method and were normalized with respect to the absorption edge after energy calibration using the zero-loss peak (0 eV).

Annealing of $UO_2(acac)_2$@SWCNTs in tube furnace

The as-prepared $UO_2(acac)_2$@SWCNTs was transferred to a quartz boat and reduced in a tube furnace, which was heated from room temperature to 600 °C at a ramping rate of 25 °C min^{-1} under an H_2/Ar (100 mL min^{-1}) atmosphere, and the annealing was maintained for 2 h before natural cooling to room temperature.

Data availability

All data have been provided in the main text and ESI.†

Author contributions

F. Y. conceived this project. L. Y. Z., K. W., and X. Z. carried out the experiments. L. Y. Z. wrote the draft and F. Y. revised the manuscript. All authors contributed to data analysis, interpreted the data, and approved the final manuscript.

Conflicts of interest

The authors declare the following competing financial interest(s): F. Y. declare a financial interest: patents related to this research have been submitted. The remaining authors declare no competing financial interests.

Acknowledgements

We gratefully acknowledge the Core Research Facilities of SUSTech for characterization. This work is financially supported by the National Natural Science Foundation of China (22222504, 92161124), the National Key Research and Development Program of China (2021YFA0717400), the Shenzhen Basic Research Project (JCYJ20210324104808022), the Guangdong Provincial Natural Science Foundation (2021A1515010229), and the Guangdong Pearl River Talent Plan (2021QN02C104).

Notes and references

1 C. Onofri, C. Sabathier, C. Baumier, C. Bachelet, D. Drouan, M. Gérardin and M. Legros, *Acta Mater.*, 2020, **196**, 240–251.
2 S. J. Zinkle, K. A. Terrani, J. C. Gehin, L. J. Ott and L. L. Snead, *J. Nucl. Mater.*, 2014, **448**, 374–379.
3 D. A. Andersson, G. Baldinozzi, L. Desgranges, D. R. Conradson and S. D. Conradson, *Inorg. Chem.*, 2013, **52**, 2769–2778.
4 R. J. McEachern and P. Taylor, *J. Nucl. Mater.*, 1998, **254**, 87–121.
5 A. Soulié, G. Baldinozzi, F. Garrido and J.-P. Crocombette, *Inorg. Chem.*, 2019, **58**, 12678–12688.
6 K. Wang, L. Wang, Z. Yao, L. Zhang, L. Zhang, X. Yang, Y. Li, Y.-G. Wang, Y. Li and F. Yang, *Sci. Adv.*, 2022, **8**, eabo4599.
7 H. Zhao, Y. Zhu, H. Ye, Y. He, H. Li, Y. Sun, F. Yang and R. Wang, *Adv. Mater.*, 2023, **35**, 2206911.
8 H. Ye, Z. Zhang and R. Wang, *Small*, 2023, **19**, 2303872.
9 N. D. Loh, S. Sen, M. Bosman, S. F. Tan, J. Zhong, C. A. Nijhuis, P. Král, P. Matsudaira and U. Mirsaidov, *Nat. Chem.*, 2017, **9**, 77–82.
10 D. Kim, B. Lee, S. Thomopoulos and Y.-S. Jun, *Nat. Commun.*, 2018, **9**, 962.
11 D. Gebauer and H. Cölfen, *Nano Today*, 2011, **6**, 564–584.
12 F. C. Meldrum and C. O'Shaughnessy, *Adv. Mater.*, 2020, **32**, 2001068.
13 S. Iijima and T. Ichihashi, *Nature*, 1993, **363**, 603–605.
14 F. Yang, M. Wang, D. Zhang, J. Yang, M. Zheng and Y. Li, *Chem. Rev.*, 2020, **120**, 2693–2758.
15 L. Bocquet, *Nat. Mater.*, 2020, **19**, 254–256.
16 R. H. Tunuguntla, R. Y. Henley, Y. C. Yao, T. A. Pham, M. Wanunu and A. Noy, *Science*, 2017, **357**, 792–796.
17 H. Qu, A. Rayabharam, X. Wu, P. Wang, Y. Li, J. Fagan, N. R. Aluru and Y. Wang, *Nat. Commun.*, 2021, **12**, 310.
18 X. Pan, Z. Fan, W. Chen, Y. Ding, H. Luo and X. Bao, *Nat. Mater.*, 2007, **6**, 507–511.
19 T. Zoberbier, T. W. Chamberlain, J. Biskupek, N. Kuganathan, S. Eyhusen, E. Bichoutskaia, U. Kaiser and A. N. Khlobystov, *J. Am. Chem. Soc.*, 2012, **134**, 3073–3079.
20 K. Cao, T. W. Chamberlain, J. Biskupek, T. Zoberbier, U. Kaiser and A. N. Khlobystov, *Nano Lett.*, 2018, **18**, 6334–6339.
21 R. Senga, H. P. Komsa, Z. Liu, K. Hirose-Takai, A. V. Krasheninnikov and K. Suenaga, *Nat. Mater.*, 2014, **13**, 1050–1054.
22 L. Shi, P. Rohringer, K. Suenaga, Y. Niimi, J. Kotakoski, J. C. Meyer, H. Peterlik, M. Wanko, S. Cahangirov, A. Rubio, Z. J. Lapin, L. Novotny, P. Ayala and T. Pichler, *Nat. Mater.*, 2016, **15**, 634–639.
23 K. Zhang, Y. F. Zhang and L. Shi, *Chin. Chem. Lett.*, 2020, **31**, 1746–1756.
24 B. W. Smith, M. Monthioux and D. E. Luzzi, *Nature*, 1998, **396**, 323–324.
25 B. Fei, H. Lu, W. Chen and J. H. Xin, *Carbon*, 2006, **44**, 2261–2264.
26 J. W. Jordan, G. A. Lowe, R. L. McSweeney, C. T. Stoppiello, R. W. Lodge, S. T. Skowron, J. Biskupek, G. A. Rance, U. Kaiser, D. A. Walsh, G. N. Newton and A. N. Khlobystov, *Adv. Mater.*, 2019, **31**, 1904182.
27 X. Yang, T. Liu, R. Li, X. Yang, M. Lyu, L. Fang, L. Zhang, K. Wang, A. Zhu, L. Zhang, C. Qiu, Y.-Z. Zhang, X. Wang, L.-M. Peng, F. Yang and Y. Li, *J. Am. Chem. Soc.*, 2021, **143**, 10120–10130.

28 X. Yang, C. Zhu, L. Zeng, W. Xue, L. Zhang, L. Zhang, K. Zhao, M. Lyu, L. Wang, Y.-Z. Zhang, X. Wang, Y. Li and F. Yang, *Chem. Sci.*, 2022, **13**, 5920–5928.
29 J. W. Jordan, J. M. Cameron, G. A. Lowe, G. A. Rance, K. L. Y. Fung, L. R. Johnson, D. A. Walsh, A. N. Khlobystov and G. N. Newton, *Angew. Chem., Int. Ed.*, 2022, **61**, e202115619.
30 X. Zhao, K. Wang, G. Yang, X. Wang, C. Qiu, J. Huang, Y. Long, X. Yang, B. Yu, G. Jia and F. Yang, *J. Am. Chem. Soc.*, 2023, **145**, 25242–25251.
31 S. Zhu, L. Ding, X. Zhang, K. Wang, X. Wang, F. Yang and G. Han, *Angew. Chem., Int. Ed.*, 2023, **62**, e202309545.
32 M. Nagata, S. Shukla, Y. Nakanishi, Z. Liu, Y. C. Lin, T. Shiga, Y. Nakamura, T. Koyama, H. Kishida, T. Inoue, N. Kanda, S. Ohno, Y. Sakagawa, K. Suenaga and H. Shinohara, *Nano Lett.*, 2019, **19**, 4845–4851.
33 X. Yang, X. Zhao, T. Liu and F. Yang, *Chin. J. Chem.*, 2021, **39**, 1726–1744.
34 R. J. Kashtiban, C. E. Patrick, Q. Ramasse, R. I. Walton and J. Sloan, *Adv. Mater.*, 2022, **35**, e2208575.
35 K. Wang, G.-J. Xia, T. Liu, Y. Yun, W. Wang, K. Cao, F. Yao, X. Zhao, B. Yu, Y.-G. Wang, C. Jin, J. He, Y. Li and F. Yang, *J. Am. Chem. Soc.*, 2023, **145**, 12760–12770.
36 Y. Li, A. Li, J. Li, H. Tian, Z. Zhang, S. Zhu, R. Zhang, S. Liu, K. Cao, L. Kang and Q. Li, *ACS Nano*, 2023, **17**, 20112–20119.
37 M. Gao, Y. Park, J. Jin, P. C. Chen, H. Devyldere, Y. Yang, C. Song, Z. Lin, Q. Zhao, M. Siron, M. C. Scott, D. T. Limmer and P. Yang, *J. Am. Chem. Soc.*, 2023, **145**, 4800–4807.
38 Y. Lee, Y. W. Choi, K. Lee, C. Song, P. Ercius, M. L. Cohen, K. Kim and A. Zettl, *Adv. Mater.*, 2023, **35**, 2307942.
39 J. Du, S. Liu, Y. Liu, G. Wu, X. Liu, W. Zhang, Y. Zhang, X. Hong, Q. Li and L. Kang, *J. Am. Chem. Soc.*, 2024, **146**, 8464–8471.
40 J. W. Jordan, K. L. Y. Fung, S. T. Skowron, C. S. Allen, J. Biskupek, G. N. Newton, U. Kaiser and A. N. Khlobystov, *Chem. Sci.*, 2021, **12**, 7377–7387.
41 K. Cao, T. Zoberbier, J. Biskupek, A. Botos, R. L. McSweeney, A. Kurtoglu, C. T. Stoppiello, A. V. Markevich, E. Besley, T. W. Chamberlain, U. Kaiser and A. N. Khlobystov, *Nat. Commun.*, 2018, **9**, 3382.
42 Y. Sun, H. Zhao, D. Zhou, Y. Zhu, H. Ye, Y. A. Moe and R. Wang, *Nano Res.*, 2019, **12**, 947–954.
43 Y. Cao, Y. Sun, H. Yang, L. Zhou, Q. Huang, J. Qi, P. Guan, K. Liu and R. Wang, *Nano Lett.*, 2023, **23**, 1211–1218.
44 D. S. Su, B. Zhang and R. Schlögl, *Chem. Rev.*, 2015, **115**, 2818–2882.
45 K. Cao, J. Biskupek, C. T. Stoppiello, R. L. McSweeney, T. W. Chamberlain, Z. Liu, K. Suenaga, S. T. Skowron, E. Besley, A. N. Khlobystov and U. Kaiser, *Nat. Chem.*, 2020, **12**, 921–928.
46 F. Yang, H. Zhao, W. Wang, Q. Liu, X. Liu, Y. Hu, X. Zhang, S. Zhu, D. He, Y. Xu, J. He, R. Wang and Y. Li, *CCS Chem.*, 2021, **3**, 154–167.
47 X. Zhao, S. Sun, F. Yang and Y. Li, *Acc. Chem. Res.*, 2022, **55**, 3334–3344.
48 R. Wang, *Nat. Catal.*, 2020, **3**, 333–334.
49 W. Yuan, B. Zhu, X.-Y. Li, T. W. Hansen, Y. Ou, K. Fang, H. Yang, Z. Zhang, J. B. Wagner, Y. Gao and Y. Wang, *Science*, 2020, **367**, 428–430.
50 H. Frey, A. Beck, X. Huang, J. A. van Bokhoven and M. G. Willinger, *Science*, 2022, **376**, 982–987.
51 F. Yang, H. Zhao, R. Li, Q. Liu, X. Zhang, X. Bai, R. Wang and Y. Li, *Sci. Adv.*, 2022, **8**, eabq0794.
52 L. Wang, L. Zhang, L. Zhang, Y. Yun, K. Wang, B. Yu, X. Zhao and F. Yang, *Nano Res.*, 2023, **16**, 2209–2217.
53 L. Zhang, L. Zhang, B. Yu, R. Wang and F. Yang, *J. Phys. D: Appl. Phys.*, 2023, **56**, 413001.
54 H. Roder, E. Hahn, H. Brune, J. P. Bucher and K. Kern, *Nature*, 1993, **366**, 141–143.
55 J. P. Bucher, E. Hahn, P. Fernandez, C. Massobrio and K. Kern, *Europhys. Lett.*, 1994, **27**, 473–478.
56 D. Seo, J. H. Park, J. Jung, S. M. Park, S. Ryu, J. Kwak and H. Song, *J. Phys. Chem. C*, 2009, **113**, 3449–3454.
57 M. Tang, W. T. Yuan, Y. Ou, G. X. Li, R. Y. You, S. D. Li, H. S. Yang, Z. Zhang and Y. Wang, *ACS Catal.*, 2020, **10**, 14419–14450.
58 T. H. Lim, D. McCarthy, S. C. Hendy, K. J. Stevens, S. A. Brown and R. D. Tilley, *ACS Nano*, 2009, **3**, 3809–3813.
59 F. Cheng, L. Lian, L. Li, J. Rao, C. Li, T. Qi, Z. Zhang, J. Zhang and Y. Gao, *Adv. Sci.*, 2019, **6**, 1802202.
60 L. Gan, R. Yu, J. Luo, Z. Cheng and J. Zhu, *J. Phys. Chem. Lett.*, 2012, **3**, 934–938.
61 H. Liu, Y. Zhang, L. Zhang, X. Mu, L. Zhang, S. Zhu, K. Wang, B. Yu, Y. Jiang, J. Zhou and F. Yang, *J. Am. Chem. Soc.*, 2024, **146**, 20193–20204.
62 L. Zhang, Y. Li, L. Zhang, K. Wang, Y. Li, L. Wang, X. Zhang, F. Yang and Z. Zheng, *Adv. Sci.*, 2022, **9**, 2200592.
63 F. Yang, H. Zhao, W. Wang, L. Wang, L. Zhang, T. Liu, J. Sheng, S. Zhu, D. He, L. Lin, J. He, R. Wang and Y. Li, *Chem. Sci.*, 2021, **12**, 12651–12660.
64 J. Zheng, D. Meng, J. Guo, X. Liu, L. Zhou and Z. Wang, *Adv. Mater.*, 2024, **36**, 2405129.